Supplementary Information

Direct Observation of a Plasmon-Induced Hot Electron Flow in a Multimetallic Nanostructure

Lars van Turnhout[1], Yocefu Hattori[1], Jie Meng[2], Kaibo Zheng[2,3], Jacinto Sá[1,4]*

[1] Physical Chemistry Division, Department of Chemistry, Ångström Laboratory, Uppsala University, 75120 Uppsala, Sweden

[2] Department of Chemistry, Technical University of Denmark, DK-2800 Kongens Lyngby, Denmark

[3] Chemical Physics and NanoLund, Lund University, Box 124, 22100 Lund, Sweden

[4] Institute of Physical Chemistry, Polish Academy of Sciences, 01-224 Warsaw, Poland

*jacinto.sa@kemi.uu.se

Materials

All reagents and materials used were purchased from commercial vendors and used as received. Silver nitrate ($AgNO_3$, ≥ 99%), polyvinylpyrrolidone (PVP, M_w ~ 10000), and
4-nitrophenol (4-NP, ≥ 98%) were obtained from Sigma-Aldrich. Sodium borohydride ($NaBH_4$,
≥ 99%) and ethylene glycol (EG, ≥ 99.5%) were purchased from Fluka Analytical. Sodium hydroxide (NaOH, ≥ 98%) was obtained from Fisher Chemicals. Acetone (≥ 99%) was bought from VWR Scientific. Titanium dioxide paste (TiO_2, Ti-Nanoxide T/SP, 15-20 nm particles) and zirconium paste (ZrO_2, Zr-Nanoxide Z/SP, 20-40 nm particles) were obtained from Solaronix. 24K gold was utilized for evaporations. Doubly-deionized water was used in all experiments.

Instrumentation

Characterization

Optical absorption (UV-Vis) were recorded using a setup equipped with a deuterium-tungsten-halogen light source (DH-2000-BAL, Ocean Optics) and a USB4000 spectrometer (Ocean Optics). ATR-FTIR spectra were recorded on a Perkin–Elmer Spectrum one FT-IR spectrometer using Universal ATR sampling Accessory. Samples

were analyzed in reflectance mode in the range between 600-4000 cm^{-1}, using a 2 cm^{-1} resolution and collecting 32 scans per sample. Raman spectra were collected in a RENISHAW inVia^{TM} confocal Raman microscope using a 20x objective. Excitation was performed at 523 nm with a laser power of 10%, exposure time of 10 s and 5 acquisitions, in the range of 200-4000 cm^{-1}. Dynamic light scattering (DLS) measurements were carried out in a Malvern NanoS machine and a total of 3 measurements comprised of 12 scans each was performed per sample. Transmission electron microscopy (TEM) measurements were conducted on a FEI Titan Analytical 80-300ST TEM from FEI Company. Scanning electron microscope energy-dispersive X-ray spectroscopies (SEM-EDS) studies were performed by QFEG 200 Cryo ESEM under 30 kV accelerating voltage.

Transient absorption spectroscopy (TAS)

Transient absorption experiments were conducted using a Ti:sapphire amplifier with integrated oscillator and pump lasers (Libra LHE, Coherent Inc.) and Transient Absorption Spectrometer (TAS, Newport Corp.). The output of a Ti:sapphire amplifier with integrated oscillator and pump lasers (800 nm, 40 fs, 3 kHZ, Libra LHE, Coherent Inc.) was split into two beams. Excitation pulses were created using an optical parametric amplifier (Topas C, Light Conversion). Probe pulses (a broad supercontinuum spectrum) were generated from the 800 nm pulses in a CaF_2 or sapphire crystal and split into a probe and reference pulse. The generated super-continuum was focused onto the sample and overlapped with the pump beam. The transient spectra were detected with a fiber-coupled CCD-based monochromator (Oriel, Newport). Pump powers of 200 μW were used, unless stated differently. The instrument response function is ca. 180-200 fs.

Transient absorption infrared spectroscopy (TIRAS)

Experiments were carried out in a femtosecond transient absorption spectrometer (Helios IR, Ultrafast Systems LLC) at room temperature. The 1 mJ, 45 fs output of a 1 kHz Ti:Sapphire amplifier (Spitfire Pro, Spectra-Physics) was split into two separate commercial optical para-metric amplifiers (TOPAS-C, Light Con-version), which

generate the visible pump and the mid-IR probe pulses. Prior to reaching the sample, the probe beam was split into equal intensity probe and reference beams using a wedged ZnSe window. Only the probe beam interacts with the photo-excited volume of the sample. All beams were focused with a single f = 10 cm off axis parabolic mirror to a 70 μm spot size in the sample. The probe and reference beams were dispersed by a commercial monochromator (Triax 190, HORIBA Jobin Yvon) equipped with a 75 groove/mm grating and detected on a dual array, 2 x 64 pixel mercury cadmium telluride detector (InfraRed Associated, Inc). Pump powers of 200 μW were used, unless stated differently. The instrument response function is around 180-200 fs.

Methods

Preparation of Ag NPs

The procedure for the preparation of Ag NPs was adapted from the well-known polyol process[1]. In short, $AgNO_3$ (0.2041 g, 1.2 mmol) and PVP (7.0145 g) were dissolved in EG (75 mL) at room temperature under continuous stirring at 300 rpm The reaction mixture was then heated to 120 ^oC. Upon reaching the desired temperature, an aqueous solution of NaOH (4 mL, 4 mM) was injected into the solution. An aqueous solution of $NaBH_4$ (1 mM) was then added dropwise to the reaction mixture, resulting in the solution obtaining a deep brown colour. The addition of $NaBH_4$ was continued until no further colour change was observed.

The reaction mixture was stored at 4 ^oC in the dark. Washing of the Ag NPs was only performed prior to usage according to the following procedure. The Ag NPs were precipitated using acetone and the mixture was centrifuged at 5000 rpm for 5 min. A volume ratio of 1:4 between the Ag NP solution and acetone was used. The supernatant was discarded and the precipitate was dried under vacuum for 24 h. The Ag NPs were redispersed in the desired amount of H_2O, sonicated for 5 min, and centrifuged at 5000 rpm for 30 min. This resulted in precipitation of large particles and aggregates. Only the supernatant was kept after centrifugation.

Preparation of nanohybrid systems

All nanohybrid systems were prepared as films either on FTO or on ultrathin glass substrates (for TIRAS measurements). All annealing processes were carried out at 500 ^{o}C for 30 min, employing a heating ramp of 10 ^{o}C per minute. In short, for all systems, a base layer of TiO_2 paste was screen-printed and subsequently annealed. A 1 nm layer of Au was then evaporated and annealed on top. This evaporation was carried out at a pressure of 7.8 mbar and a current of 49 A was applied. A second layer of TiO_2 paste was then screen-printed on top of the Au NPs (to avoid direct contact between Ag and Au) and also annealed. The substrate was then immersed for 24 h in an aqueous solution containing the Ag NPs. For Ag-TiO_2, Ag-ZrO_2, and Au-TiO_2 systems, samples were prepared in a identical fashion but without the Au evaporation or Ag immersion step, respectively, and using the ZrO_2 paste in case of the Ag-ZrO_2 sample.

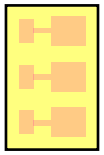

For the catalytic sample, a mask as shown on the right was used for Au evaporation to ensure both gold and silver are exposed on the surface (presence of an annealed Au monolayer was observed to prevent binding of Ag NPs on those spots).

Photocatalytic studies

The reduction of 4-nitrophenol to 4-aminophenol in the presence of $NaBH_4$ was studied using UV-Vis absorption spectroscopy. A 3 mL aqueous solution of 4-nitrophenol (8.6 x 10^{-5-} M, 1.5 mL) and $NaBH_4$ (8.6 x 10^{-3} M, 1.5 mL) was prepared. The substrate prepared as outlined in the previous subsection was placed against one of the side walls of a 4 mL volume and 1 cm pathlength quartz cuvette in such a way that it does not interfere with the spectroscopic beam (see Figure 3c for the employed set-up). The mixture including the substrate was closed air-tight and purged with argon gas for 5 min. Subsequently, the cuvette was placed inside the spectrophotometer and absorption spectra were recorded with a time interval of 2 min for a total time of 30 min.

All nanohybrid systems (Ag-TiO_2-Au, Ag-TiO_2, Au-TiO_2), as well as bare TiO_2 as a reference sample were tested both with and without laser illumination. In case of laser illumination, a 445 nm continuous wave blue laser (12 V) was used to illuminate the

substrate. All measurements were performed inside an enclosure that prevents ambient light from entering.

TAS and TIRAS signal fitting

For the kinetic traces recorded using TAS and TIRAS, fitting of the rising edge and signal decay were performed using exponential fitting function. A mono-exponential rising function (equation 1) was used to fit all rising edges:

$$S(t) = e^{-\left(\frac{t-t_0}{t_p}\right)^2} * \sum_i A_i e^{-\frac{t-t_0}{t_i}},\ t_p = \frac{IRF}{2 \cdot ln2} \quad (1)$$

where * is the convolution operator. I think is also important to mention that the time zero correction was done for each data by fitting using the IRF.

The signal decays were fitted using either a mono-exponential (equation 2) or two-exponential decay (equation 3) with an 'infinite' component:

$$\Delta A_{\text{mono}-\text{exponetial decay}} = A_1 * \exp\left(-\frac{t}{\tau_1}\right) + \Delta A_0 \quad (2)$$

$$\Delta A_{\text{two}-\text{exponential decay}} = A_1 * \exp\left(-\frac{t}{\tau_1}\right) + A_2 * \exp\left(-\frac{t}{\tau_2}\right) + \Delta A_0 \quad (3)$$

In these equations τ_1 and τ_2 are the lifetimes of the decay processes. A_1 and A_2 are the weighted coefficients that represent the contribution of each of the decay processes to the total decay. ΔA_0 represent the infinite component and is the offset.

Photocatalytic rate evaluation

Apparent catalytic rates were determined based on pseudo-first order rate analysis of the recorded absorption spectra. The 100-fold excess of $NaBH_4$ in comparison to 4-nitrophenol allows for pseudo first-order rate kinetics to be used[2]. The apparent rate constant is determined from plots of $-\ln\left(\frac{A}{A_0}\right)$ versus time t, where A is the absorbance of 4-nitrophenol (ca. 400 nm) at time t and A_0 the 4-nitrophenol absorbance at time 0. The slope obtained in these plots represents the apparent pseudo first order catalytic rate constant k_{app}.

Characterization of Ag NPs

Enlarged figures showing the TEM pictures of the silver NPs and the extracted size distribution are presented in Figure S1 and S2, respectively. The quasi-spherical particle shape is shown in the inset of Figure S1. An average size of 22.8 ± 6.8 nm was found. The recorded DLS spectrum of the silver NPs in water is shown in Figure S3, and the corresponding absorption spectrum in Figure S4.

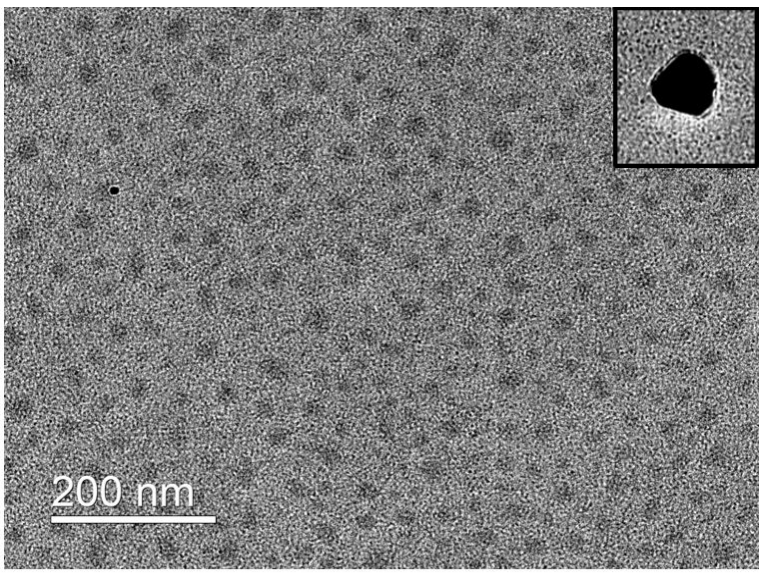

Figure S1. TEM picture of the prepared silver NPs with the inset showing the quasi-spherical particle shape.

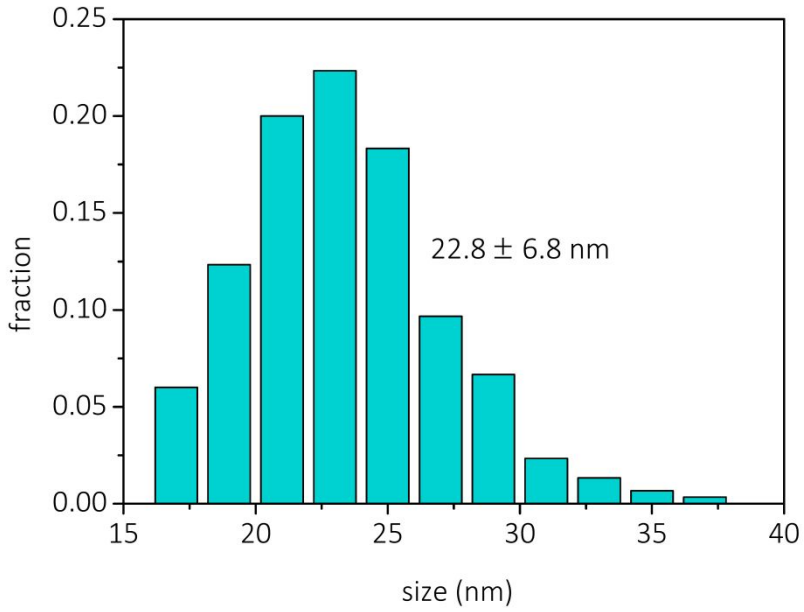

Figure S2. TEM distribution of the prepared silver NPs. An average size of 22.8 ± 6.8 nm was found.

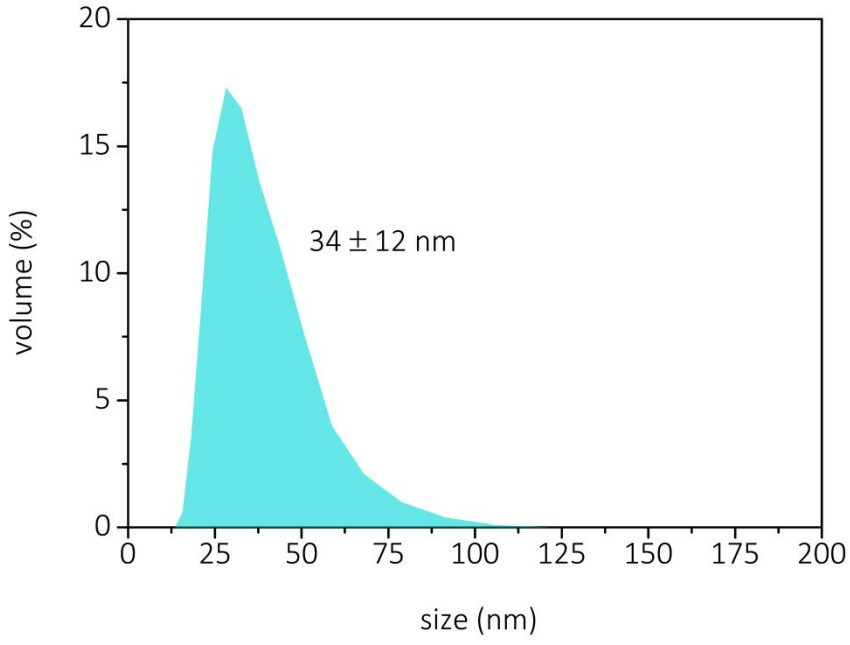

Figure S3. DLS spectrum of the prepared silver NPs in water.

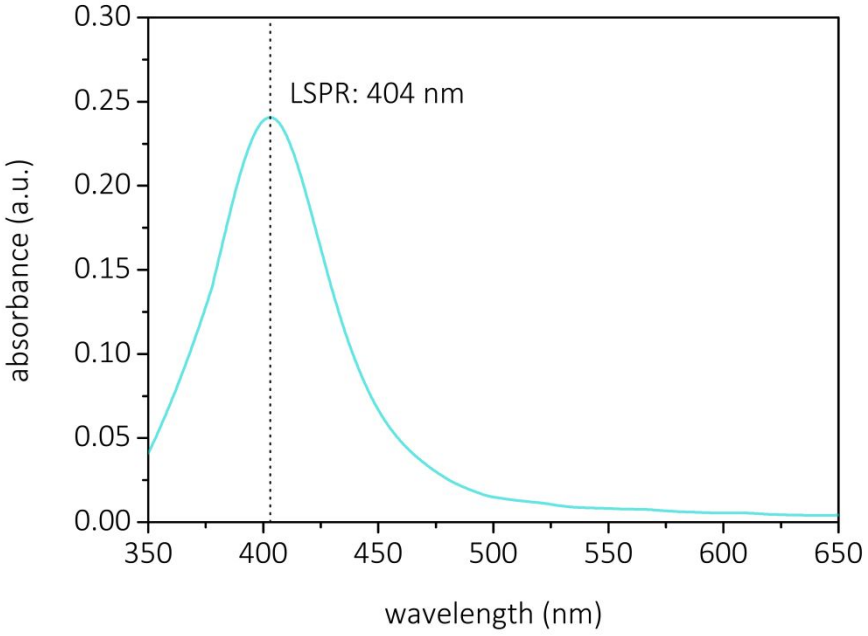

Figure S4. UV-Vis absorption spectrum of the prepared silver NPs in water.

The recorded ATR-FTIR spectra of the Ag NPs, PVP, and the $AgNO_3$ precursor are shown in Figure S5. The characteristic vibrations of PVP are indicated both in bare PVP and in the silver NPs capped in PVP.

Comparison of the PVP versus the Ag NPs spectrum shows a blue shift of 13 cm^{-1} of the C=O stretching vibration (1663 to 1650 cm^{-1}), which is indicative of coordination of the PVP to the Ag core via the oxygen atom. Furthermore, an increase in intensity in the O-H bending vibration (3600-3100 cm^{-1}) indicates keto-enol tautomerization, which is a stronger nucleophilic agent than the ketone tautomer and will more strongly coordinate to the silver core, thus further indicating coordination of PVP to silver through the oxygen atom. The fact that the characteristic C-N stretching vibrations in PVP did not shift upon coordination further indicates that the nitrogen atom is not involved in the coordination and hence coordination via the oxygen atom is most plausible.

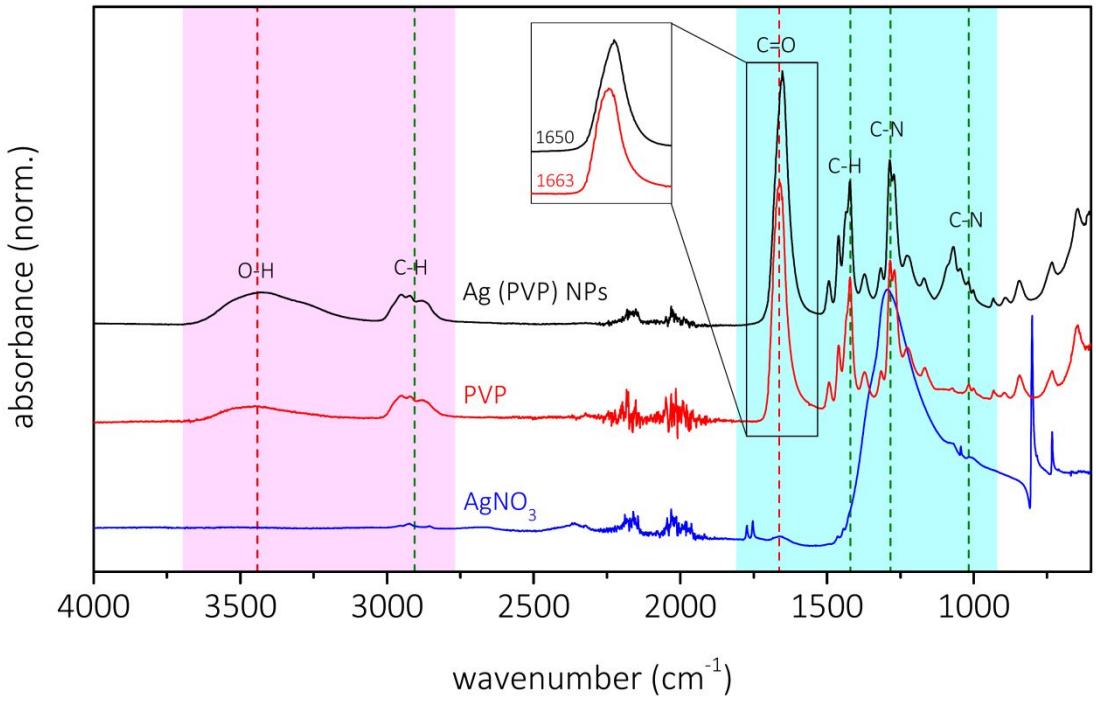

Figure S5. ATR-FTIR spectra of the prepared silver NPs, of PVP alone, and of $AgNO_3$.

The recorded Raman spectra of the Ag NPs, PVP, and the $AgNO_3$ precursor are shown in Figure S6. Again characteristic vibrations of PVP are indicated both in bare PVP and in the silver NPs capped in PVP. Two features are worth pointing out, first of all the enhanced O-H bending vibration (3600-3100 cm^{-1}) in the Ag NP spectrum. Coordination of the oxygen atom to the Ag NPs could be the reason of this peak being enhanced due to resonant effects. Secondly, a peak around 250 cm^{-1} is present in the spectrum of the Ag NPs. This peak is widely attributed to Ag-O or Ag- N bonds and based on the aforementioned observations is attributed to Ag-O and further demonstrates successful linking of the PVP capping agent to the silver NP core.

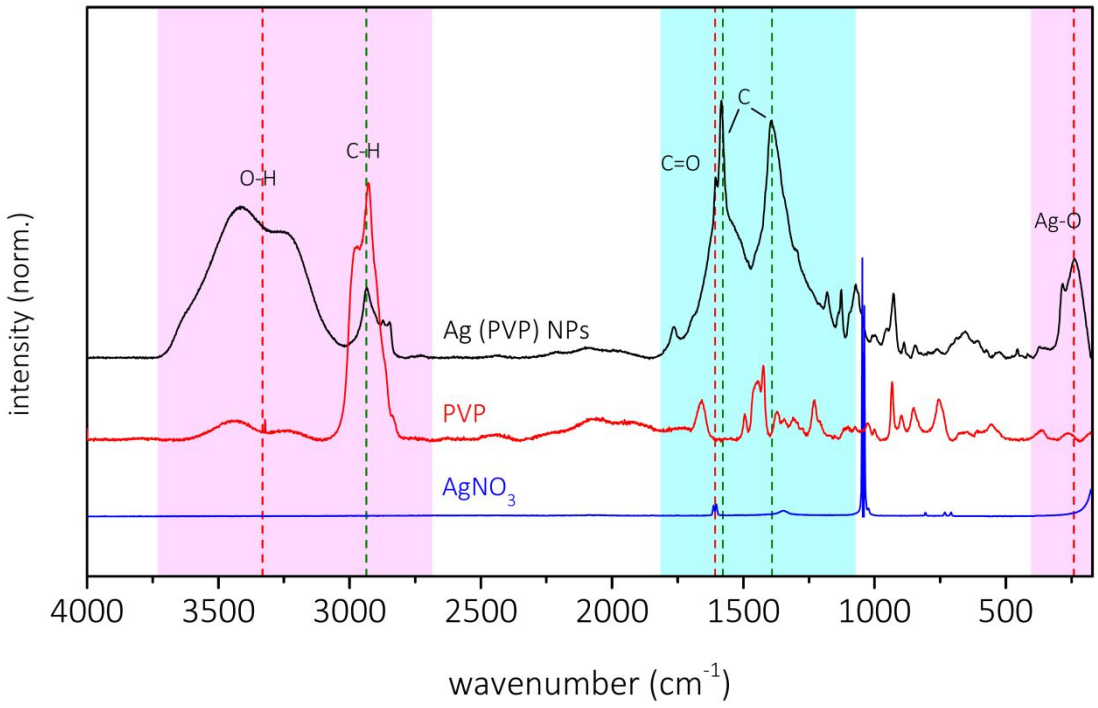

Figure S6. Raman spectra of the prepared silver NPs, of PVP alone, and of $AgNO_3$.

Characterization of Au NPs on TiO_2

The Au NPs evaporated onto TiO_2 were characterized via TEM. Enlarged figures showing the TEM pictures of the Au NPs and the extracted size distribution are presented in Figure S7 and S8, respectively. An average size of 5.3 ± 2.5 nm was found.

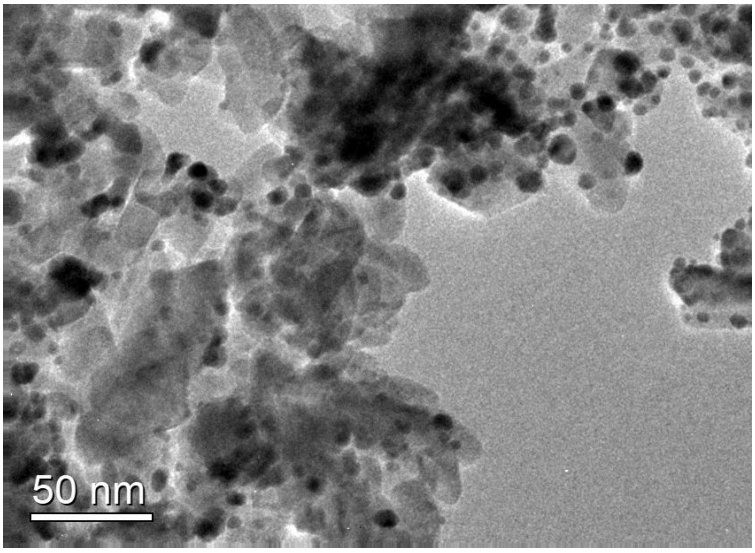

Figure S7. TEM picture of the prepared gold NPs on TiO_2.

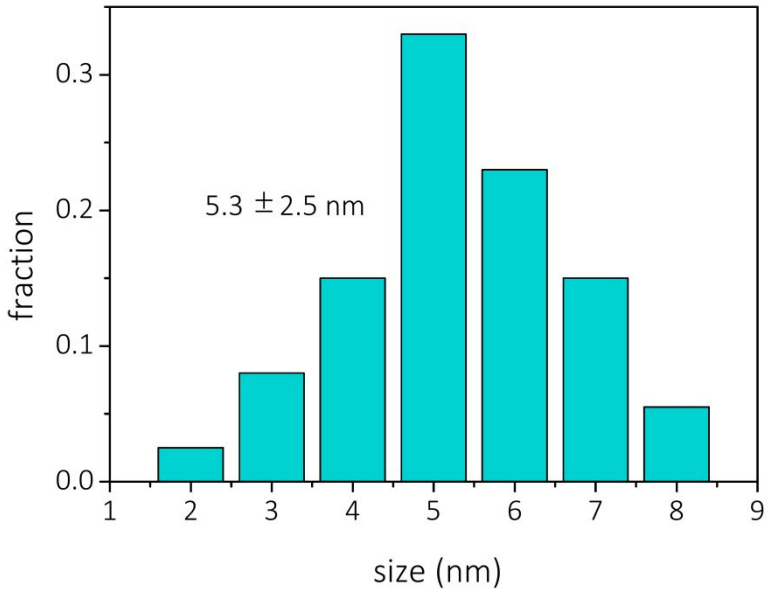

Figure S8. Size distribution of the gold NPs on TiO_2, determined via TEM. An average size of 5.3 ± 2.5 nm was found.

Characterization of the nanohybrid systems

Characterization of the multimetallic nanohybrid system was performed via UV-Vis steady-state absorption spectroscopy and by SEM-EDS analysis to quantify the ratio between Ag and Au on the sample and to assess the sample heterogeneity. Figure S9 shows the absorption spectra of the full multimetallic system and its separate components. The inset shows the absorption of the Ag NPs, as obtained by subtracting the purple from the blue line in Figure S9. From the inset, it can be observed that the LSPR peak of 404 nm (Figure S4) red-shifted to 416 nm.

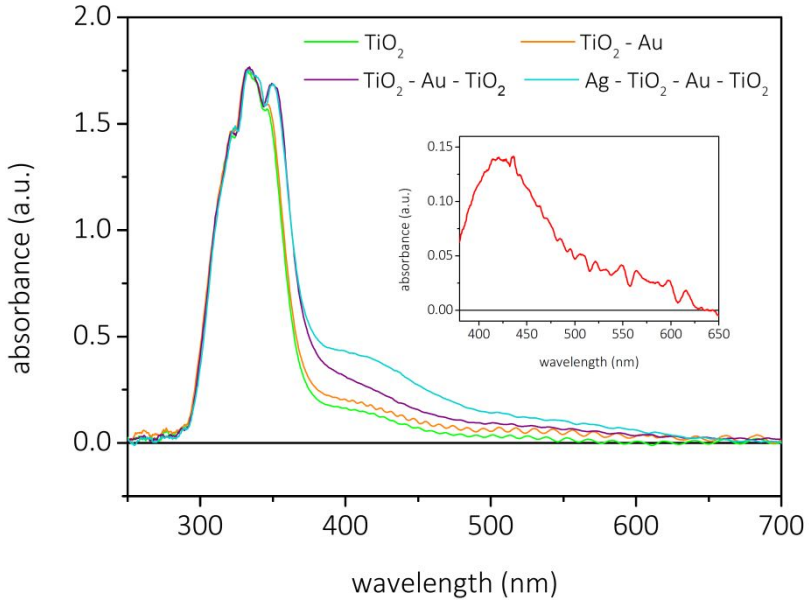

Figure S9. Absorbance spectra of the full multimetallic system, the inset shows the Ag NP absorption on the film and is obtained by subtracting the purple (TiO_2 – Au – TiO_2) from the blue (Ag – TiO_2 – Au – TiO_2) line.

In Table S1, the percentages of Ag and Au in the multimetallic nanohybrid system are presented, as obtained by SEM-EDS analysis, showing a ratio of Ag/Au of 8.4 ± 1.1 and indicating the formation of a relatively homogeneous film.

Table S1. Percentages silver and gold in the multimetallic Ag-TiO_2-Au system determined on 10 random sites together with the Ag/Au ratio per site and average Ag/Au ratio.

Site	Percentage Ag (%)	Percentage Au (%)	Ag/Au ratio
1	90.1	9.9	9.1
2	89.6	10.4	8.6
3	89.2	10.8	8.4
4	88.1	11.9	7.4
5	91.0	9.0	10.1
6	89.0	11.0	8.1
7	88.2	11.8	7.5
8	90.9	9.1	10.0
9	89.0	11.0	8.1
10	86.7	13.3	6.5

average	8.4 ± 1.1

In Figure S10, the absorption spectra of the Au-TiO_2 sample is shown. The inset is obtained by subtracting the green from the orange line in Figure S10. The inset line was smoothed using a Savitzky-Golay filter so that the characteristic absorption of Au NPs with a plasmonic LSPR peak around 550 nm and the interband transition region at wavelengths below 500 nm can be seen more clearly.

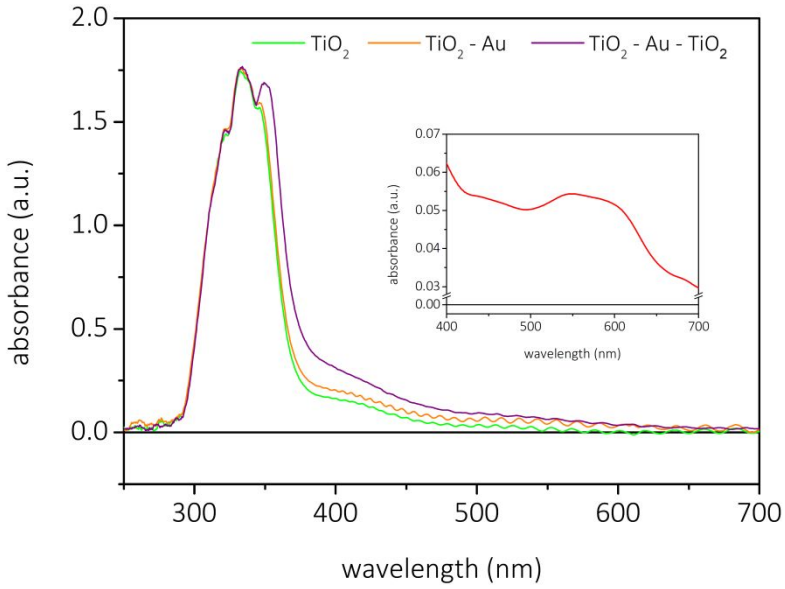

Figure S10. Absorbance spectra of the Au-TiO_2 sample, the inset shows the Au NP absorption and is obtained by subtracting the green (TiO_2) from the orange (TiO_2 – Au) line.

Figure S11 shows the absorption spectra of the Ag-TiO_2 sample, the inset showing the absorption of the Ag NPs obtained by subtracting the purple from the blue line in Figure S11.

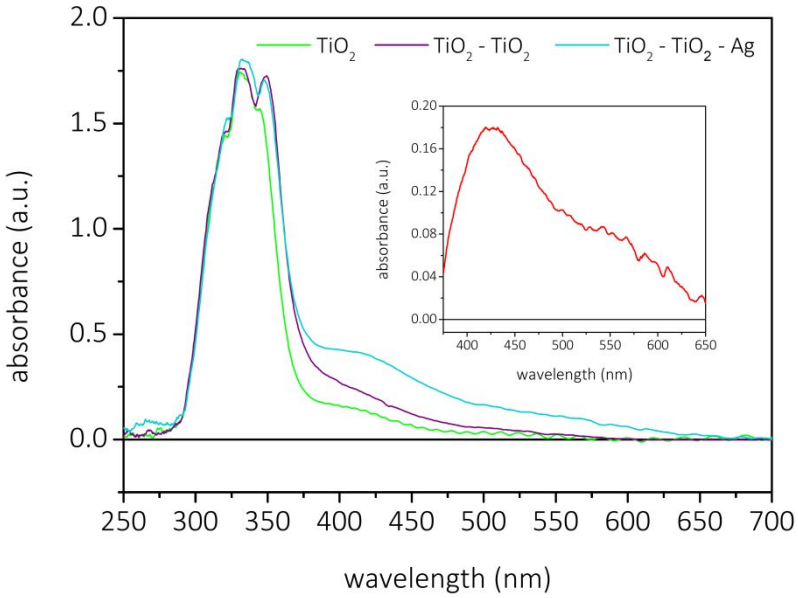

Figure S11. Absorbance spectra of the Ag-TiO_2 sample, the inset shows the Ag NP absorption and is obtained by subtracting the purple (TiO_2 – TiO_2) from the blue (TiO_2 – TiO_2 – Ag) line.

Determination of the excitation wavelength

In order to determine the pump excitation wavelength used in this study, two factors were considered. Firstly, since Ag NPs are used as the photosensitizer, it is important to excite at or near the LSPR peak. Secondly, the Au NPs, which are designed to be the catalytic site, have an overlapping absorbance with the LSPR peak of silver (see Figure 1d). The absorption of Au in this region is mainly due to interband transitions[4]. Exciting such interband transitions results in a change in the electronic distribution inside the Au NPs and subsequently a change in its absorption spectrum, thus giving rise to a signal in TAS measurements.

To determine the excitation wavelength, the signal observed in TAS experiments following exciting of Au NPs on the Au-TiO_2 sample in the region from 400-480 was evaluated. Measurements were performed at a pump power of 500 μW to obtain a clearer signal for the Au NP monolayer. Briefly, 10 scans per excitation wavelength were recorded and the maximum average bleach amplitude was extracted. The results

of this study are shown in Figure S12 (purple), together with the normalized absorbance of Ag NPs in the multimetallic nanohybrid system (blue; see Figure 1d and Figure S9 for reference). As can be seen, the maximum bleach amplitude decreases continuously from 400 to 480 nm, which is attributed to shorter wavelength inducing a larger number of interband transitions[4], hence giving rise to a larger signal. Based on these results, a wavelength of 435 nm was selected as the excitation wavelength as it provided the best comprise between exciting Ag near its LSPR and having a reduced signal due to direct Au excitations.

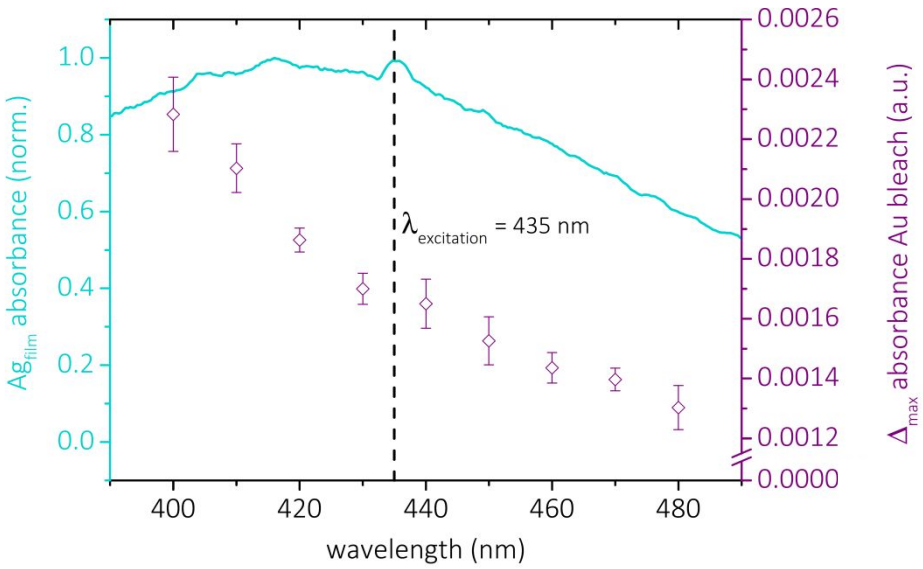

Figure S12. Normalized absorbance of the silver NPs in the complete multimetallic system (blue) and the maximum absolute ΔA value of the gold NP bleach in the Au-TiO_2 sample when excited at wavelength from 400 to 480 nm. Measurements performed at fixed laser power to estimate signal ration between Ag plasmon and Au interband.

Transient absorption data of TiO_2

To confirm that the broad high wavelength feature observed in Figure 2b and 2c (instead of the decaying winglet observed in Figure 2a for the non-injectable Ag-ZrO_2

reference sample) can be attributed to electron injection, a TiO_2 sample was studied using TAS in the visible region using an excitation wavelength of 330 nm (100 μW power). This wavelength was chosen to ensure the band-gap of TiO_2 is overcome and to ensure the creation of electrons in the TiO_2 conduction band. A sample comprised of two layers of TiO_2 was used in order to most closely resemble the other samples used for TAS experiments.

The resulting spectra are shown in Figure S13. As can be clearly seen, a strong positive feature above 480 nm, that increases across the measured wavelength range, is present. In order to validate that this feature must come from conduction band electrons, we pumped the same sample at 435 nm and, as shown in Figure S14, no signal was observed in the same region, thereby supporting our idea that the observed broad high wavelength signal seen in Figure 2b and 2c indicates electron injection into the TiO_2 conduction band.

A TiO_2 sample was also measured in the mid-infrared region following excitation at 435 nm to fully rule out the direct excitations of electrons into the TiO_2 conduction band at this wavelength. Figure S15 shows the kinetic trace at extracted at 5200 nm following excitation at 435 nm. As in Figure S14, no rise or any other type of signal is observed, thus confirming that an excitation wavelength of 435 nm does not lead to the creation of electrons in the TiO_2 conduction band.

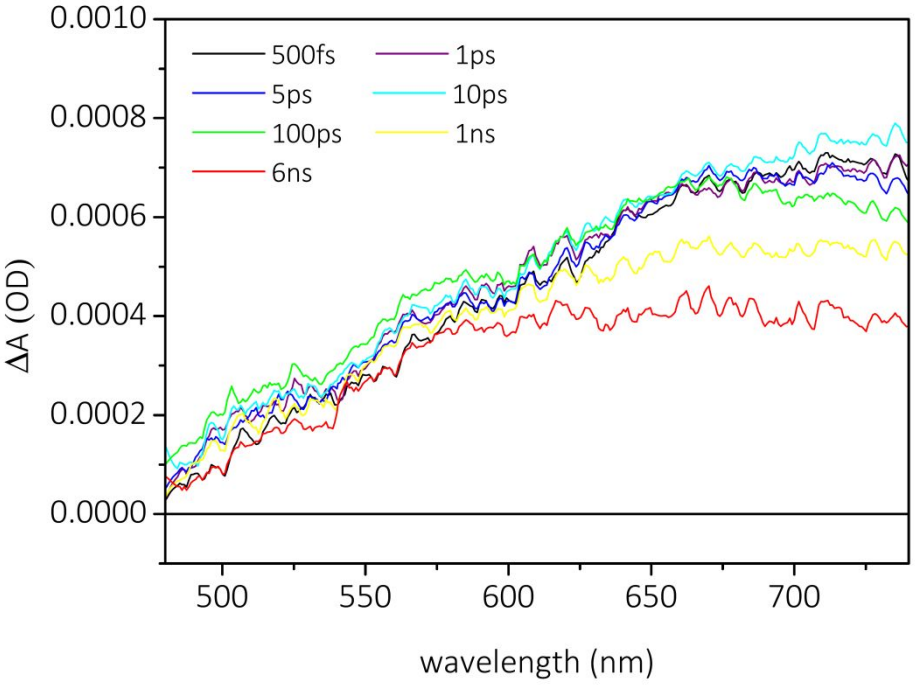

Figure S13. Transient absorption spectra of TiO_2 pumped at 330 nm (100 μW).

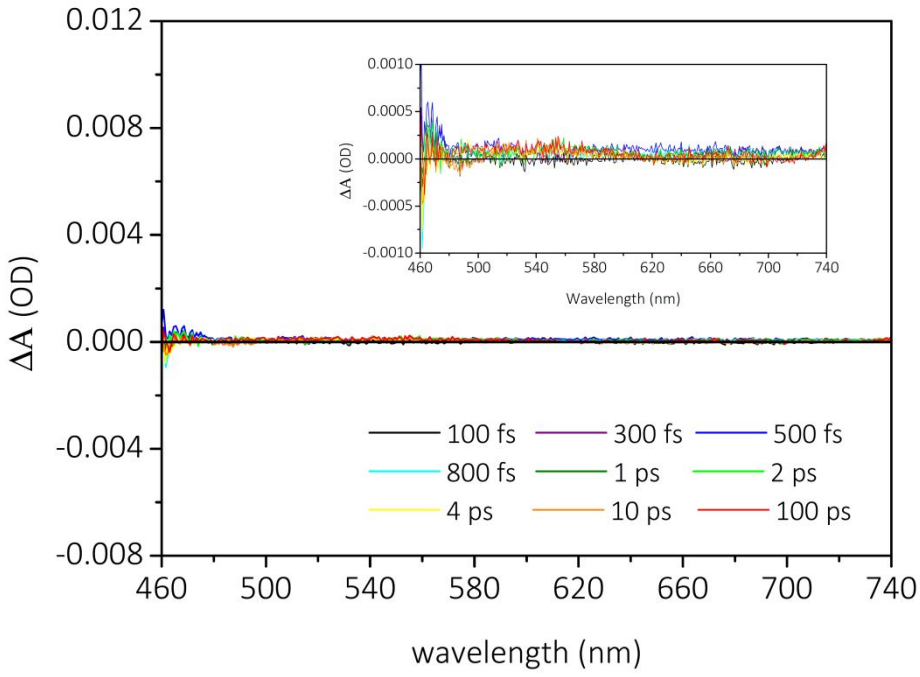

Figure S14. Transient absorption spectra of TiO_2 pumped at 435 nm. The spectrum is presented using the same scale as used in Figure 2a-c. The inset shows a zoomed version of the spectra.

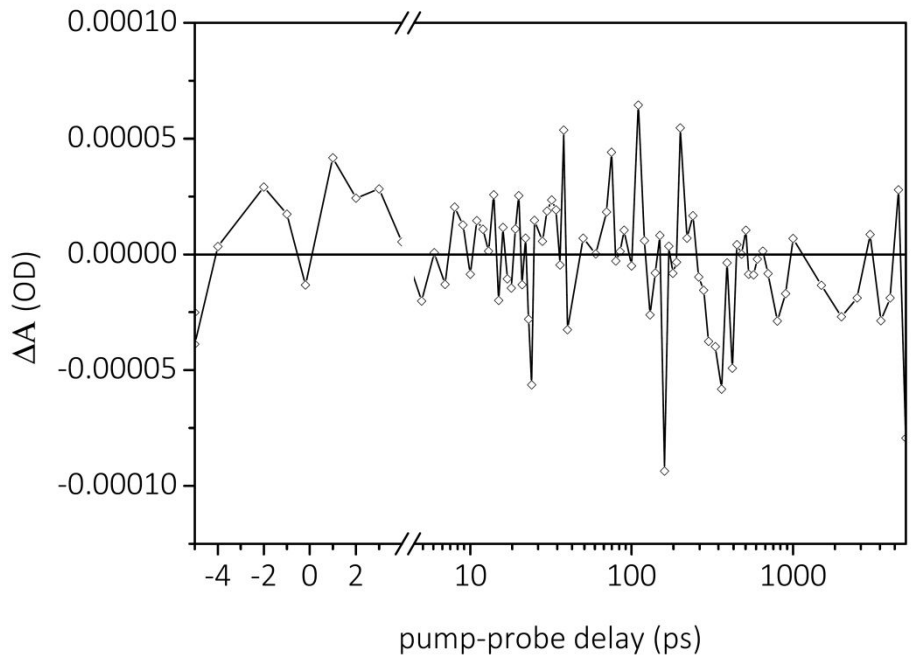

Figure S15. Kinetic traces at 5200 nm for TiO_2 system pumped at 435 nm. Dots have been connected for clarity.

Transient absorption data of Au-TiO_2

In Figure S16, the transient absorption spectra of the Au-TiO_2 sample pumped at 435 nm are presented. In Figure S17, the corresponding bleach (550 nm) and high wavelength winglet (665 nm) kinetics are evaluated. Both decays were fitted using a mono-exponential decay function with an infinite component. Time constants of 1.4 and 1.6 ps were found for the bleach and winglet, respectively. The inset shows the kinetic traces on a comparable scale as used in Figure 2f. Rising times below our IRF were found for both the bleach and winglet.

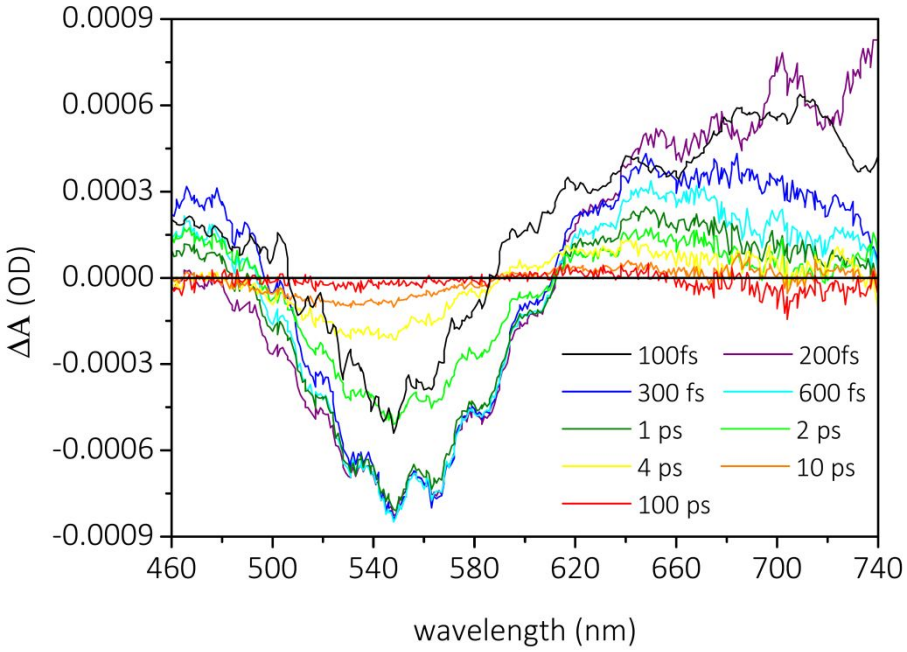

Figure S16. Transient absorption spectra of the Au-TiO_2 sample pumped at 435 nm.

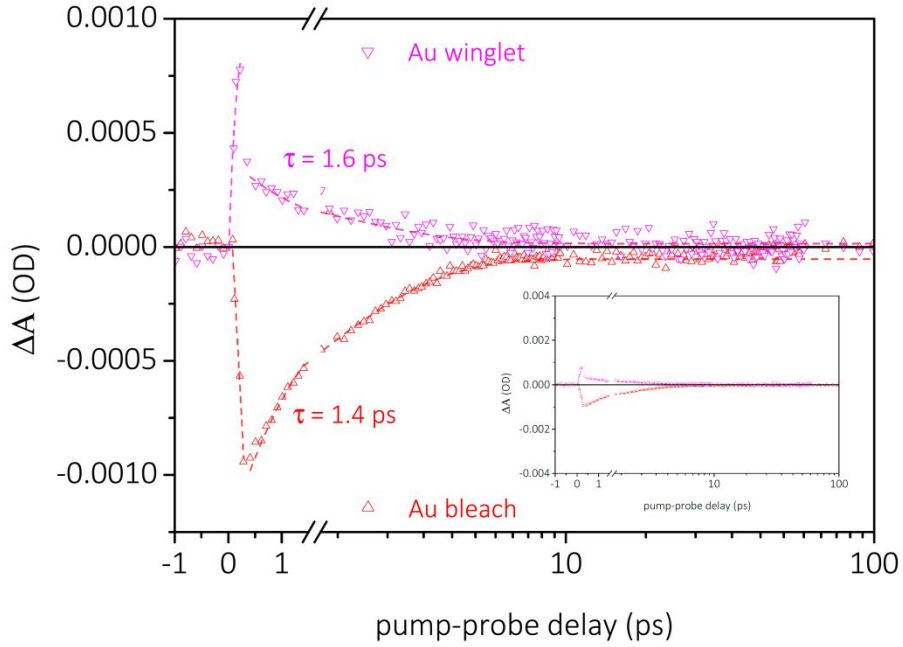

Figure S17. Kinetic traces at 550 nm (Au bleach) and 665 nm (Au winglet) nm for Au-TiO_2 sample pumped at 435 nm.

Power dependence measurements

In Figure S18-S20, the results of the power dependence studies for the Ag-TiO_2-Au, Ag-TiO_2, and Au-TiO_2, respectively, are presented in detail. Since it was decided based upon the TAS studies in the visible region that values at 0.6 ps were to be extracted,

all power dependence measurements were conducted at short pump-probe delay times up to 10 ps only. Laser powers of 25, 50, 75, 100, 125, 150, 200, and 250 μW were used for each sample.

Fitting of the obtained short time scale results was done using a mono-exponential decay function with an infinite component. The choice for a mono-exponential decay function on these short delay times is motivated by the decays presented in Figure 3b, showing a mono-exponential decay function suffices at these short times.

Figures S21-S23 present the values extracted in the power dependence measurements (similarly to Figure 4b) for the Ag-TiO_2-Au, Ag-TiO_2, and Au-TiO_2 sample, respectively. Error bars based on 20 scans per power have been included in these Figures.

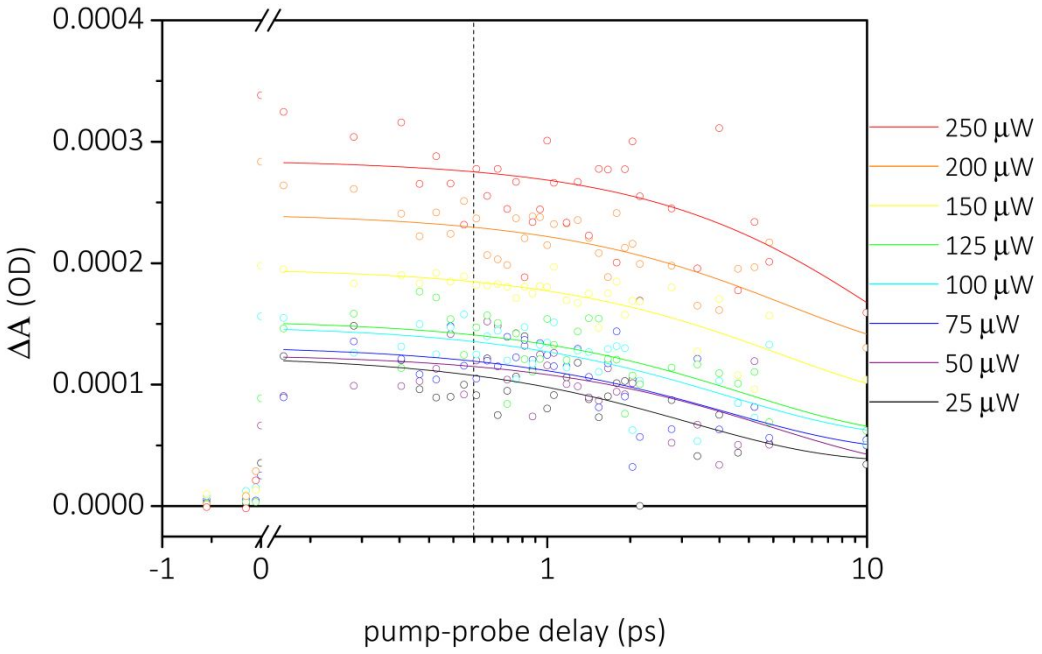

Figure S18. Kinetic traces at 5200 nm for the full multimetallic Ag-TiO_2-Au sample at various pump powers.

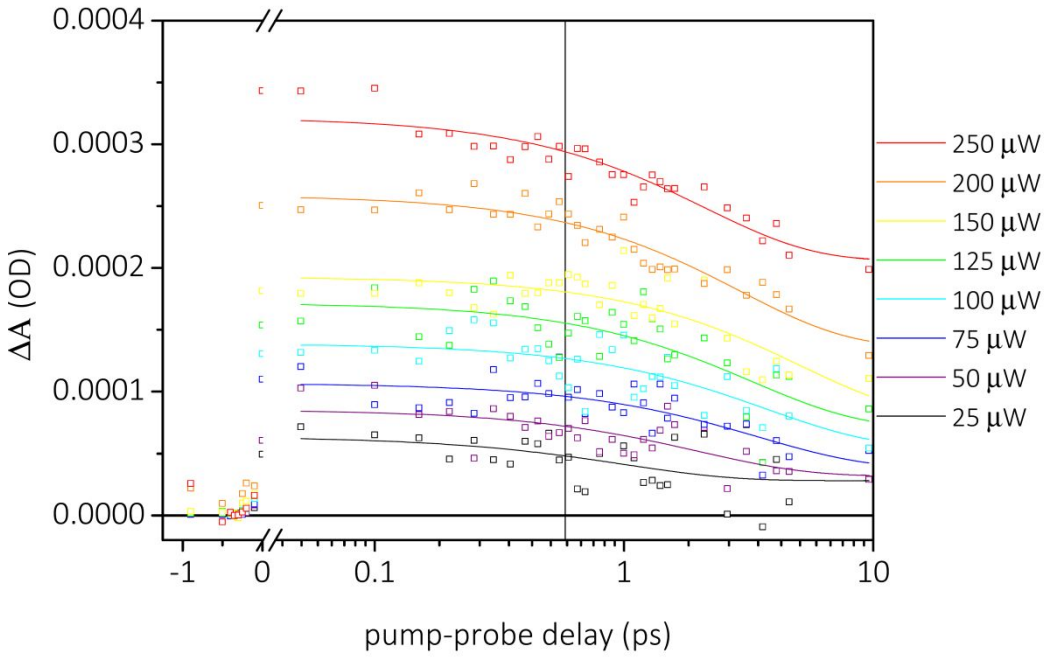

Figure S19. Kinetic traces at 5200 nm for the Ag-TiO_2 sample at various pump powers.

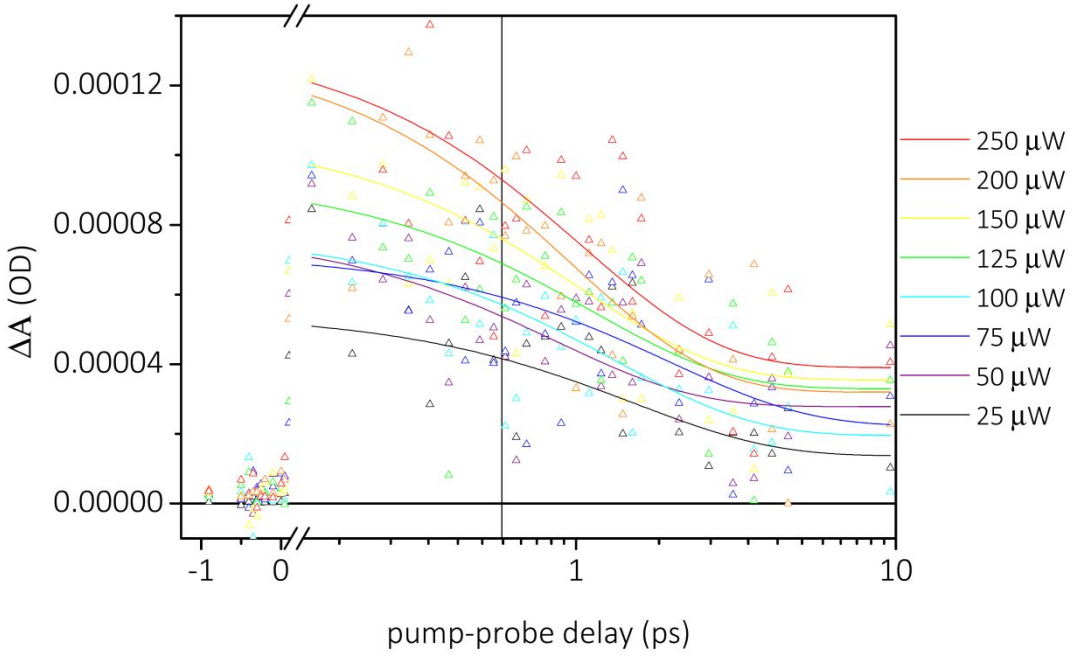

Figure S20. Kinetic traces at 5200 nm for the Au-TiO_2 sample at various pump powers.

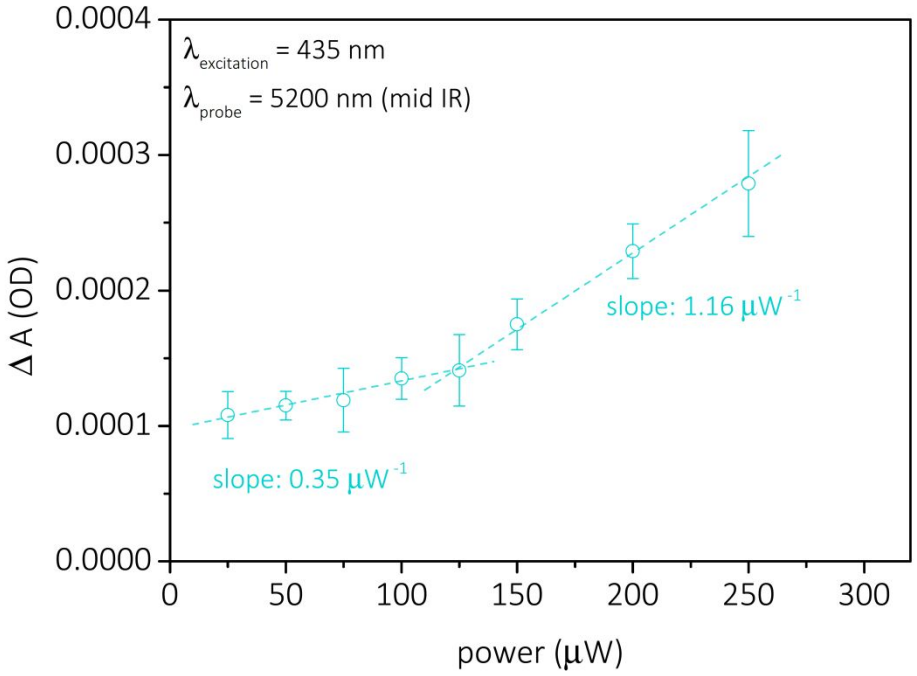

Figure S21. Power dependence measurements on the Ag-TiO_2-Au sample.

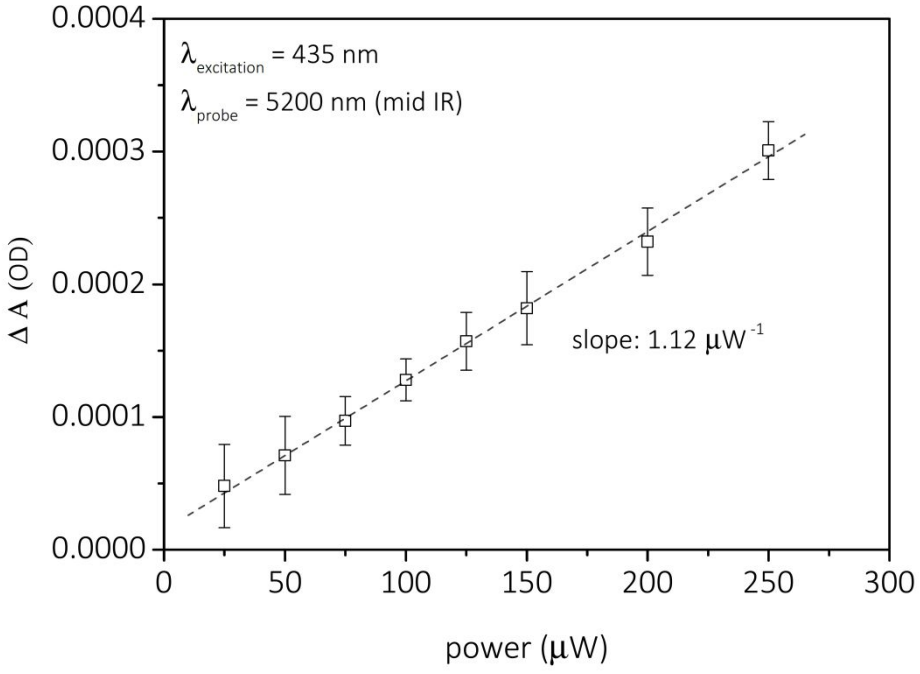

Figure S22. Power dependence measurements on the Ag-TiO_2 sample.

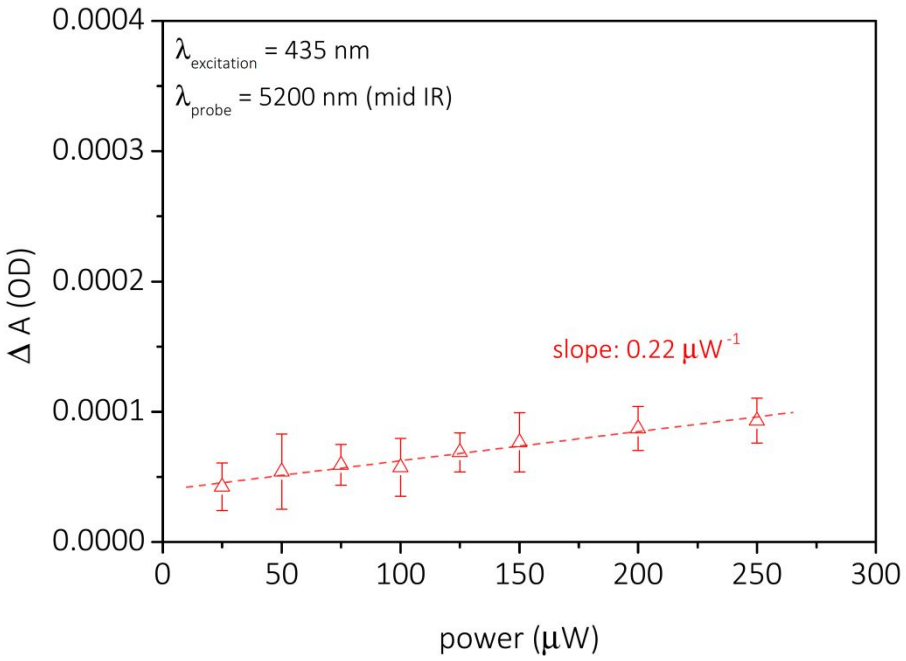

Figure S23. Power dependence measurements on Au-TiO_2 sample.

Reverse electron flow

Experiment targeting the reverse electron flow in the multimetallic Ag-TiO_2-Au system, i.e. from Au to Ag, were carried out. An excitation wavelength of 550 nm, matching the Au LSPR, was used for these experiments. All measurements were again carried out at identical fluences. The results of these studies are presented below.

Figure S24 and S25 show the transient absorption spectra of Au-ZrO_2 and Au-TiO_2, respectively. The same legend applies to both figures. In the presence of TiO_2 (Figure S25) a broad feature in the high wavelength region from 640-740 nm is visible, which is not observed for the ZrO_2 reference and again suggest electron injection upon excitation of Au-TiO2 and Au-TiO2-Ag at 550 nm.

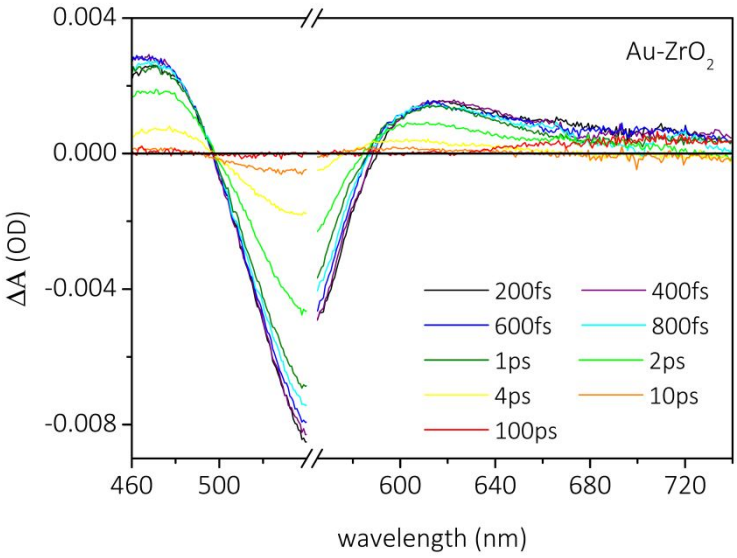

Figure S24. Transient absorption spectra of Au-ZrO_2; excited at 550 nm.

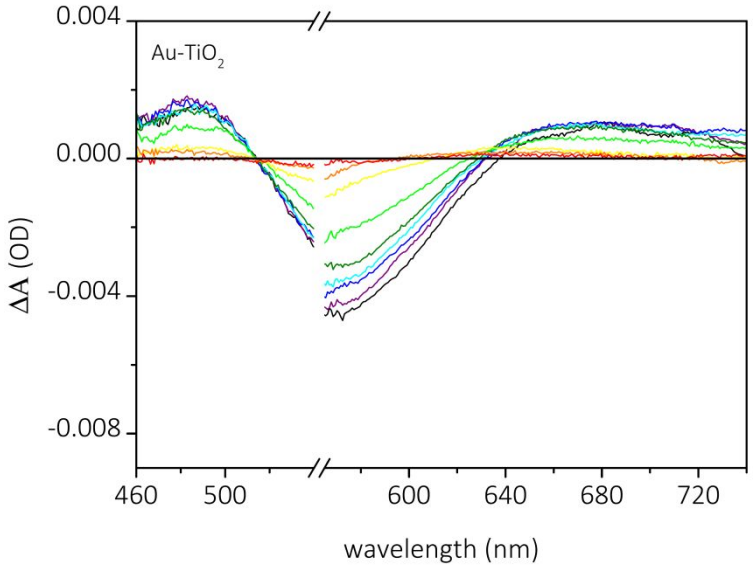

Figure S25. Transient absorption spectra of Au-TiO_2; excited at 550 nm.

Figure S26 shows the transient absorption spectra of the full Au-TiO_2-Ag system excited at 550 nm. A similar broad feature in the high wavelength region as for the Au-TiO_2 sample (Figure S25) is observed. This is attributed to electrons reaching the Ag NPs, giving rise to a broad winglet. Changes in the electronic structure of Ag are further apparent from the bleaching feature observed in the region from 460-520 nm, where the characteristic Ag bleach is dominant over the Au winglet (compare Figure S26 and S25).

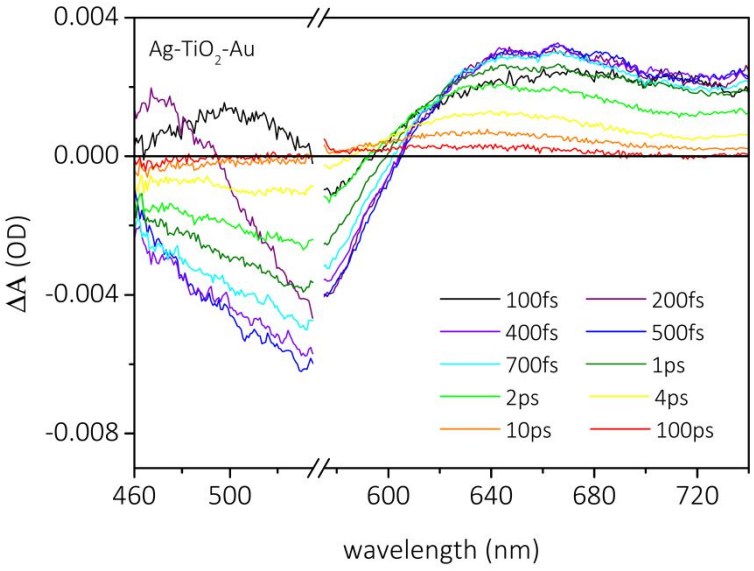

Figure S26. Transient absorption spectra of Au-TiO_2-Ag; excited at 550 nm.

Kinetic traces extracted at 530 nm, where the Au bleach occurs, are shown in Figure S27. A mono-exponential decay function was used to describe the observed decay which showed a faster electron cooling time for the full multimetallic system than for the Au-TiO_2 sample, which is in excellent agreement with the observations made when these same systems where excited at the Ag LSPR and similar explanations as presented in the main body of the paper are applicable to rationalize this trend.

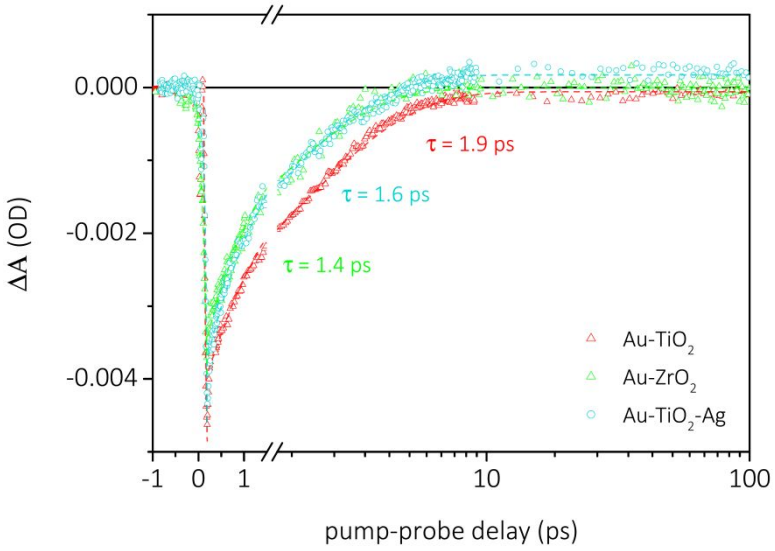

Figure S27. Kinetic traces extracted at 530 nm from Figure S24, S25, and S26.

In order to study electron injection without any spectral overlap, measurements were conducted in the mid-infrared regime too. The kinetic traces for the Au-TiO_2 and Au-TiO_2-Ag samples are found in Figure S28. A three-exponential decay function was used to describe the decay of the Au-TiO_2-Ag sample, whilst a two-exponential decay function with an infinite lifetime component was used to fit the decay of the Au-TiO_2 substrate, for which electrons surviving for longer than the length of our delay, 5 ns, were observed. Comparison of the decays of the two samples shows large decreases in all three-time constants when Ag is present. This is again attributed to the presence of a new decay site (Ag NPs) that electrons that were created on Au and injected into TiO_2 can move to.

The reductions in lifetimes are much larger than those observed when the Ag LSPR was excited (see Figure 3b). This is expected since the amount of Ag in the studied sample is significantly larger than the amount of Au (see Table S1). Hence, a larger

fraction of the created hot electrons on Au can be transferred to Ag NPs, explaining the large difference in decay kinetics.

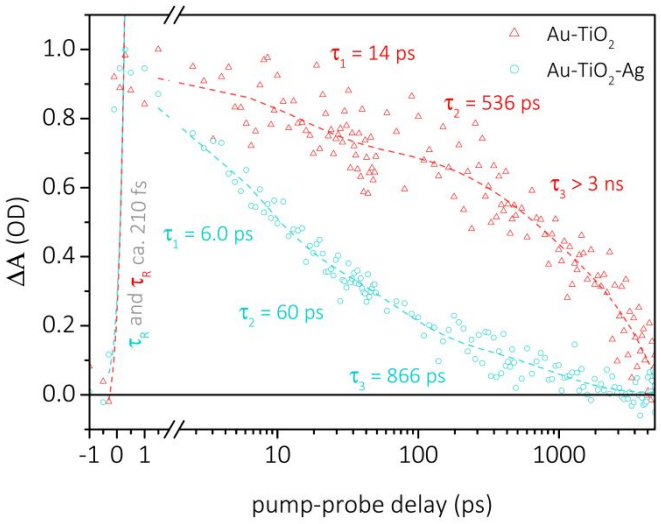

Figure S28. Kinetic traces extracted at 5200 nm from the transient infrared absorption spectra of Au-TiO_2 and Au-TiO_2-Ag.

Figure S29 shows the difference spectrum between Au-TiO_2-Ag and Au-TiO_2, revealing the characteristic Ag TAS response. The associated kinetics of the Ag bleach and winglet of the difference spectrum are shown in Figure S30. Figure S31 shows the kinetics of the Ag-TiO_2 excited at 550 nm for comparison.

The signal amplitudes of the Ag difference spectra are significantly larger than the amplitudes of the Ag-TiO_2 spectra, indicating again a larger number of hot carriers on the Ag NPs following photoexcitation of the Au LSPR. Whilst significant changes in the decay constants were observed when exciting the Ag LSPR, the changes in decay constants between Figure S30 and S31 are minor in this case, with only slightly slower decays observed for the full system. This is most likely due to the presence of a large excess of Ag versus Au, resulting in the electrons from Au being distributed over a larger number of Ag NPs, thereby only causing minor changes in the e-ph cooling times indicated by this decay constant.

The observed time lag before the signal rises compared to direct excitation of the Ag-TiO_2 sample is only on the order of 150-200 fs and is significantly shorter than when the reversed electron was studied, which could again be related to the excess of Ag NPs, resulting in a reduced time for electrons to reach the Ag site. This short time further strengthens the hypothesis of Ag NPs being present in the mesoporous TiO_2 channels and that Ag NPs are present is larger amounts making it easier for electrons to find them. Based on these results, it is clear that reversing the electron was achieved by changing the excitation wavelength so that the LSPR of Au NPs instead of Ag is excited.

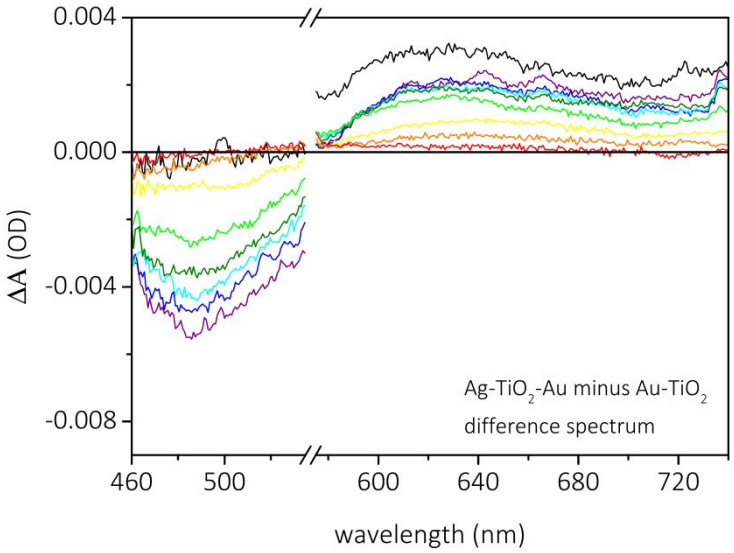

Figure S29. Difference transient absorption spectra obtained by subtracting Figure S25 from S26.

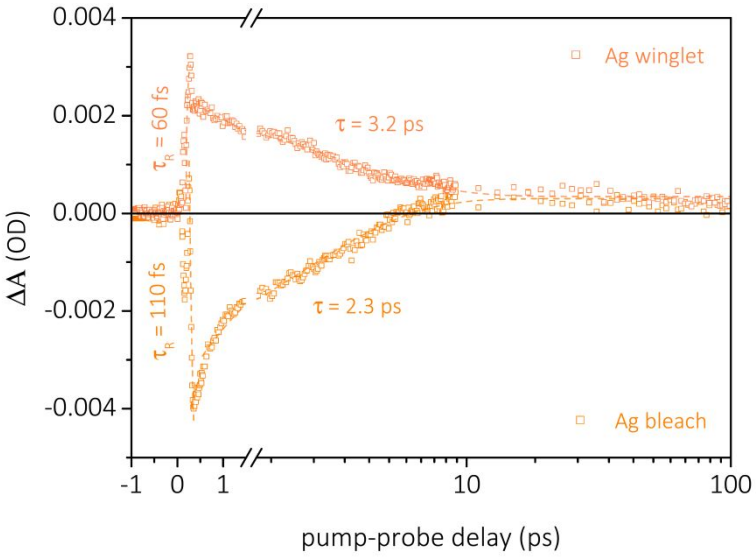

Figure S30. Kinetic traces at 530 nm and 630 nm of the difference spectrum from Figure S29.

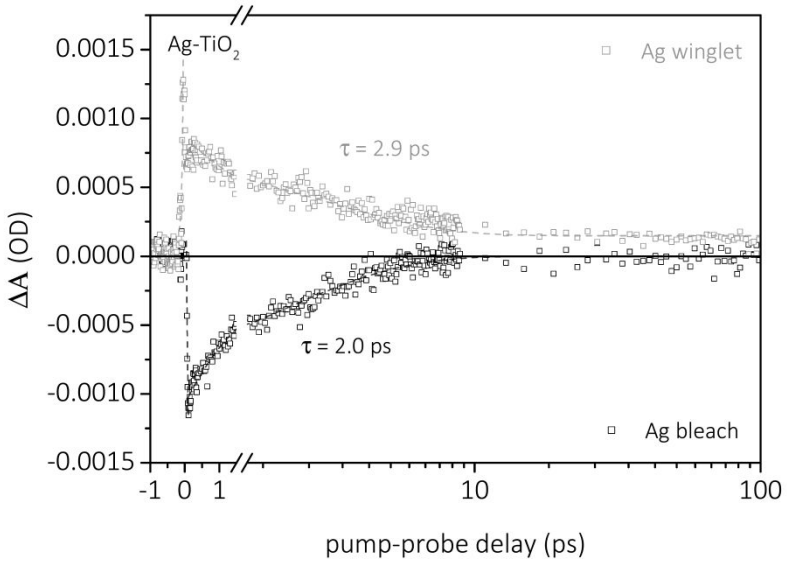

Figure S31. Kinetic traces at 530 nm and 630 nm of the Ag-TiO_2 sample excited at 550 nm.

Catalytic experiments

In Figure S32-S34, the catalytic rates evaluated in the first 600 seconds of the reaction are presented for the Ag-TiO_2-Au, Ag-TiO_2, and Au-TiO_2 sample, respectively. Addition of $NaBH_4$ to 4-nitrophenol leads to conversion of 4-nitrophenol to 4-nitrophenolate, which is a strong absorption around 400 nm. The product, 4-aminophenol, has a significantly lower extinction coefficient and absorbs around 300 nm. Due to the higher

extinction coefficient of 4-nitrophenol, the decrease in the peak absorption of this compound was used for rate analyses to determine the apparent first-order rate constants[2].

Graphs both with and without 445 nm laser radiation are presented and the apparent first order rate constants are included. Figure S35-S40 present the absorption data that the analysis in Figures S32-S34 is based on. In Figure S41 and S42, the UV-Vis absorption evaluation of the studied reaction in the presence of a TiO_2 film are presented both with and without 445 nm laser radiation, respectively. As can be seen, on the timescale of the experiments, the reaction rate in these cases is negligible.

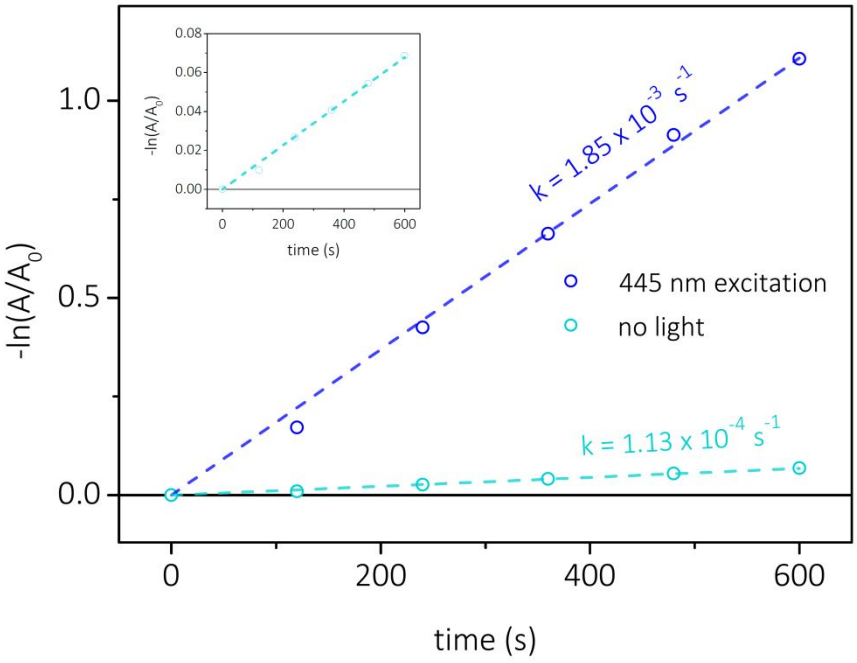

Figure S32. First-order apparent catalytic rate evaluation of the Ag-TiO_2-Au sample. The inset shows an enlarged version of this measurement in dark ('no light') conditions.

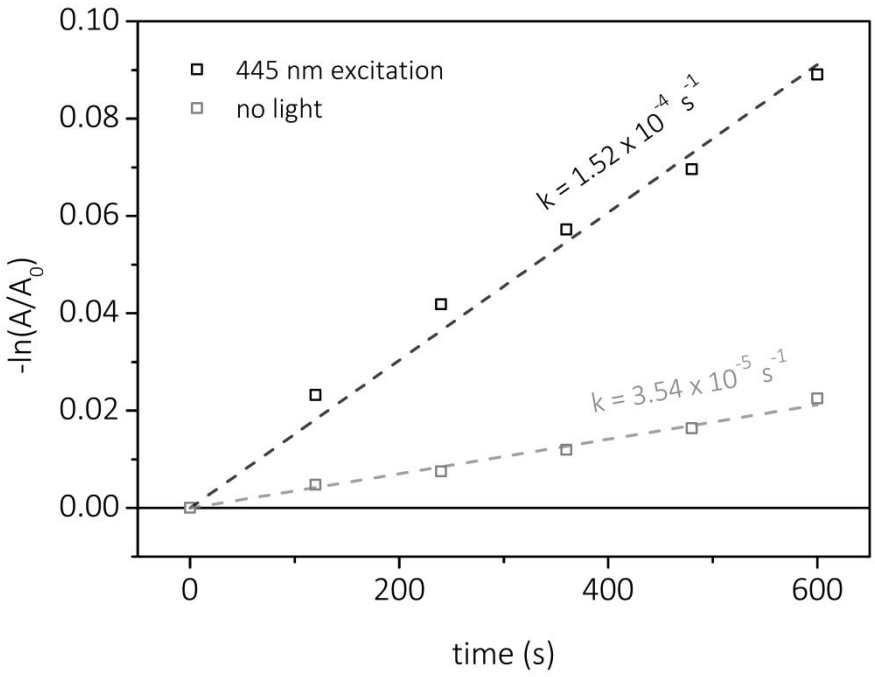

Figure S33. First-order apparent catalytic rate evaluation of the Ag-TiO_2 sample.

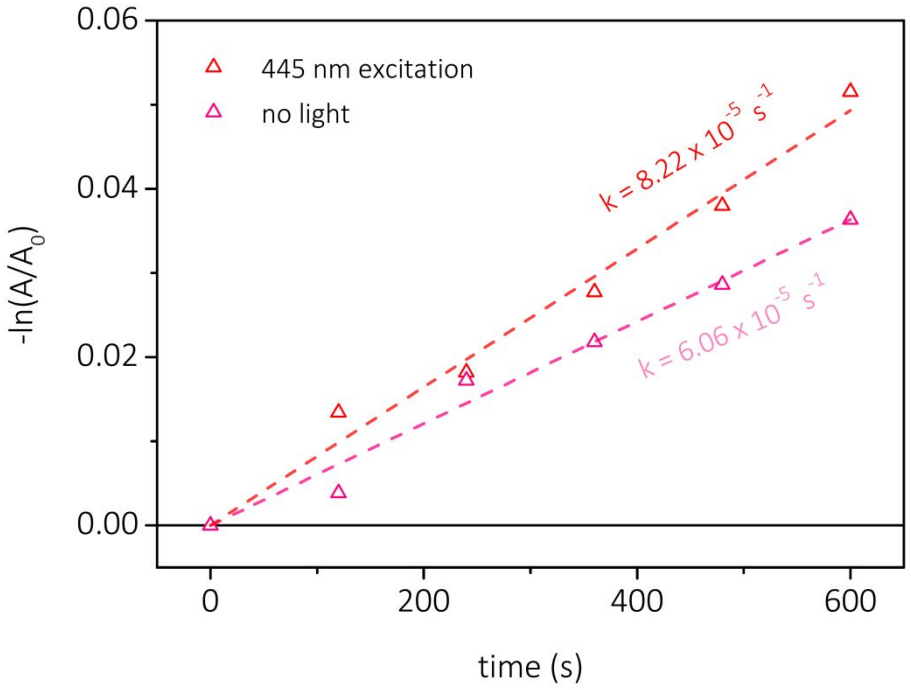

Figure S34. First-order apparent catalytic rate evaluation of the Au-TiO_2 sample.

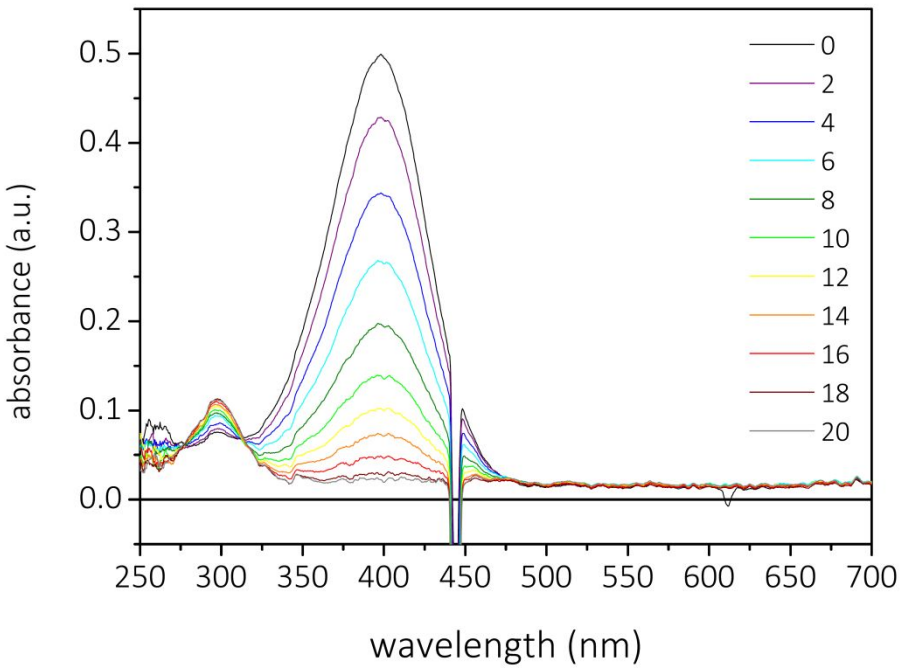

Figure S35. Recorded UV-Vis absorption spectra for the Ag-TiO_2-Au sample under 445 nm laser radiation. The legend presents the time in minutes.

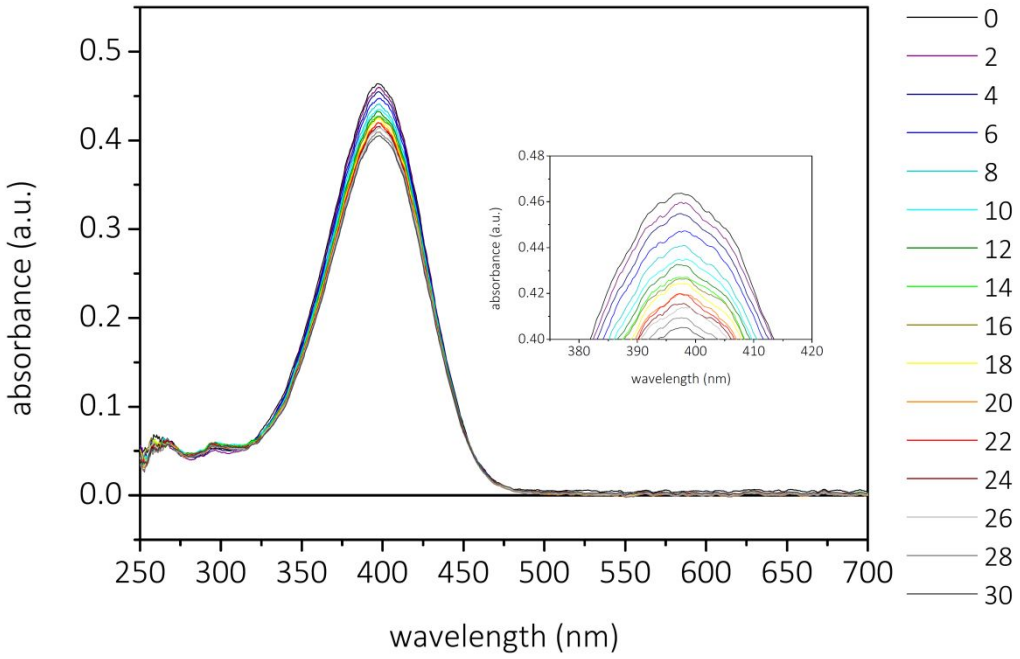

Figure S36. Recorded UV-Vis absorption spectra for the Ag-TiO_2-Au sample without laser radiation. The legend presents the time in minutes.

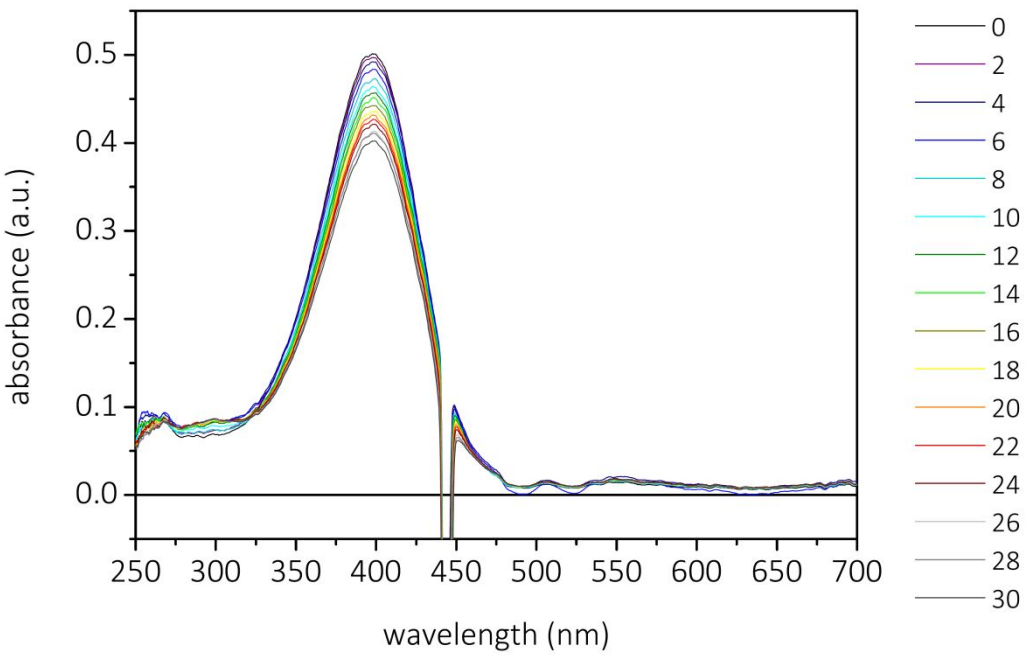

Figure S37. Recorded UV-Vis absorption spectra for the Ag-TiO_2 sample under 445 nm laser radiation. The legend presents the time in minutes.

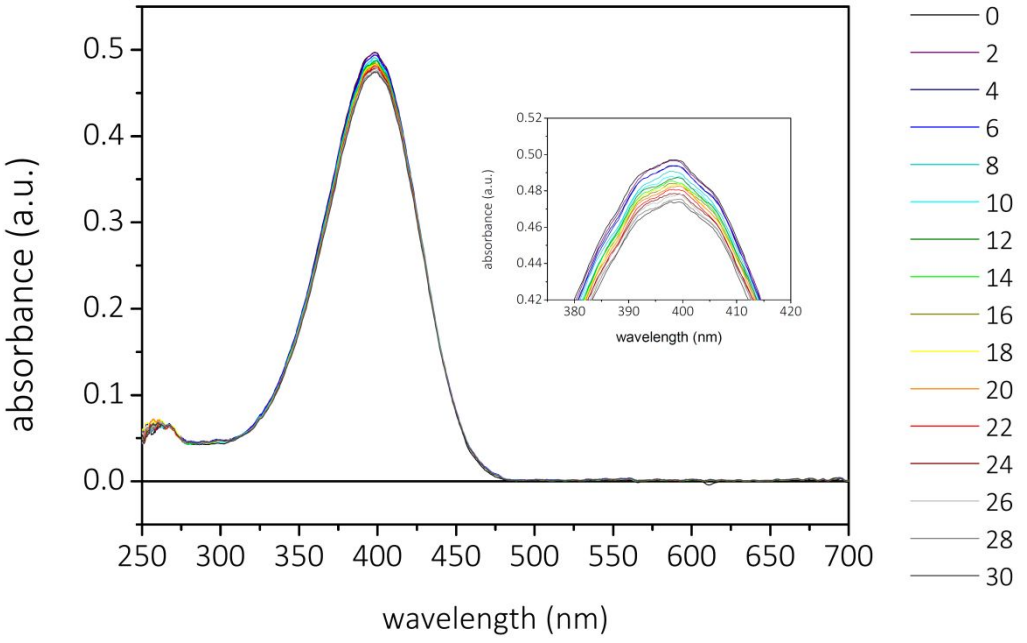

Figure S38. Recorded UV-Vis absorption spectra for the Ag-TiO_2 sample without laser radiation. The legend presents the time in minutes.

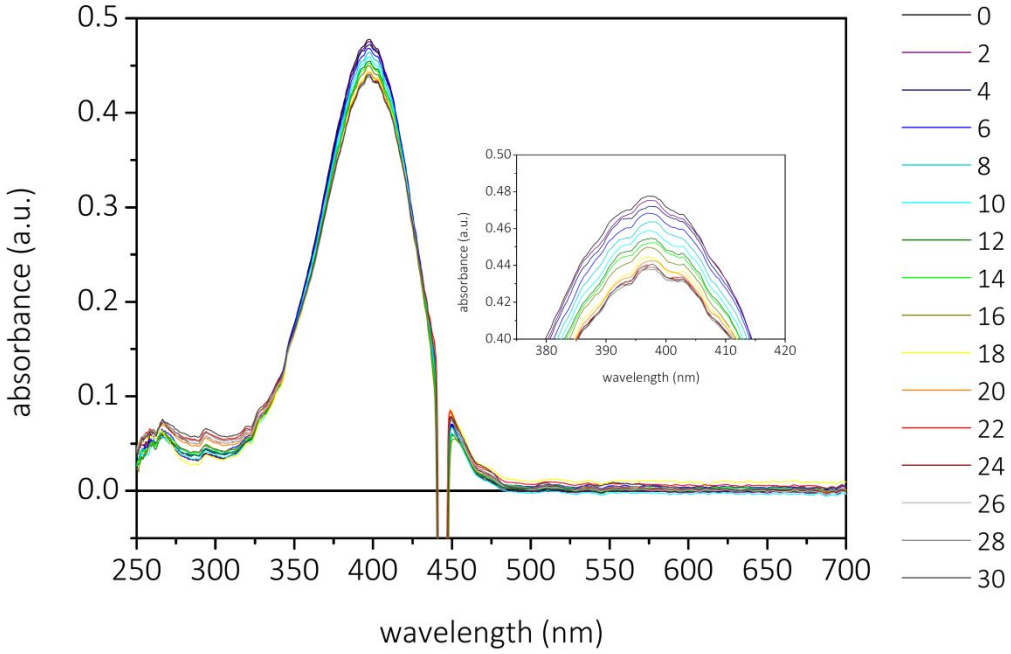

Figure S39. Recorded UV-Vis absorption spectra for the Au-TiO_2 sample under 445 nm laser radiation. The legend presents the time in minutes.

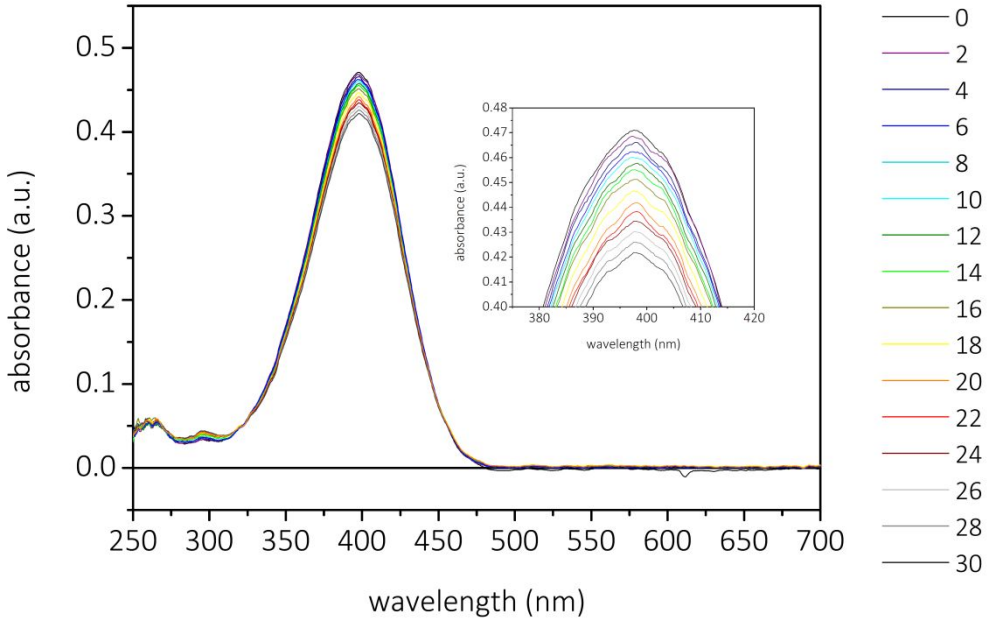

Figure S40. Recorded UV-Vis absorption spectra for the Au-TiO_2 sample without laser radiation. The legend presents the time in minutes.

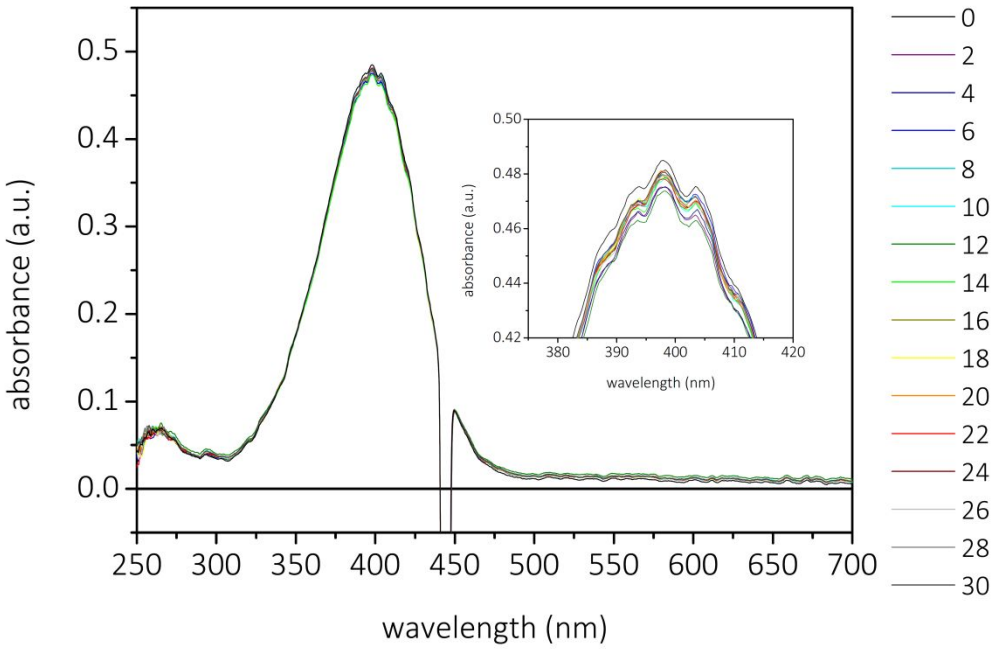

Figure S41. Recorded UV-Vis absorption spectra for the TiO_2 sample under 445 nm laser radiation. The legend presents the time in minutes.

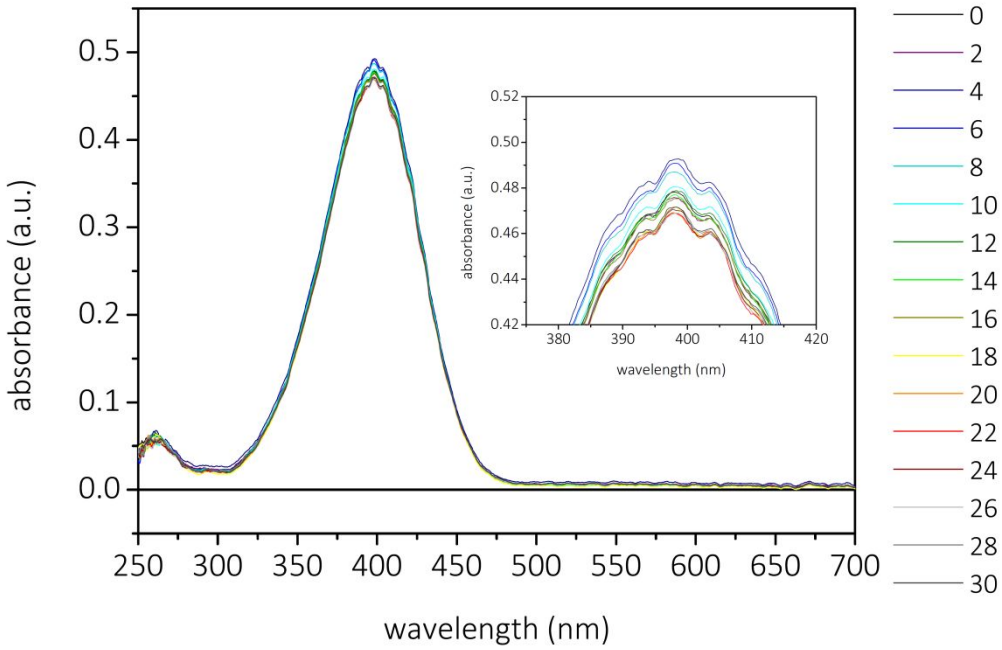

Figure S42. Recorded UV-Vis absorption spectra for the TiO_2 sample without laser radiation. The legend presents the time in minutes.

References

1. Silvert, P.-Y., et al. Preparation of colloidal silver dispersions by the polyol process. *J. Mater. Chem.* **6**, 573-577 (1996).

2. Li, M., Chen, G. Revisiting catalytic model reaction p-nitrophenol/$NaBH_4$ using metallic nanoparticles coated on polymeric spheres. *Nanoscale* **5**. 11919-11927 (2013).

3. Mirzaei, A., et al. Characterization and optical studies of PVP-capped silver nanoparticles. *J. Nanostructure Chem.* **7**, 37-46 (2017).

4. Bernardi, M. et al. Theory and computation of hot carriers generated by surface plasmon polaritons in noble metals. *Nat. Commun.* **6**, 1-9 (2015).